A Global Analytical Representation of the Magnetic Field Produced by the Region 2 Birkeland Currents and the Partial Ring Current

N. A. TSYGANENKO[1]

Laboratory for Extraterrestrial Physics, NASA Goddard Space Flight Center, Greenbelt, Maryland

A quantitative model is developed of the magnetic field produced by the electric current system of region 2 Birkeland currents, closed via the partial ring current. The distribution of $j_\perp$ is computed from a given axially asymmetric spatial distribution of hot isotropic magnetospheric plasma over an infinitely thin L shell in an axisymmetric purely dipolar geomagnetic field, while the field-aligned current density is found from the continuity of the net electric current. The magnetic field distribution is derived by a Biot-Savart integral over the electric current system. An assumed cosine dependence of the plasma pressure on local time makes it possible to reduce the problem of analytical representation of the B field to two dimensions. The obtained numerical fits for the partial ring current/region 2 Birkeland current magnetic field are relatively simple, continuous, and valid throughout the whole extraterrestrial space from ionospheric heights up to tens of R_E. To our knowledge, this is a first global analytical representation for the magnetic field of the partial ring current system which can be incorporated in future advanced models of the external geomagnetic field.

INTRODUCTION

Large-scale Birkeland current systems carry a significant fraction of the net magnetospheric electric current and hence should have a considerable effect upon the overall structure and mapping of the geomagnetic field lines. The importance of an explicit inclusion of the field-aligned current systems in global quantitative magnetospheric B field models has been emphasized in earlier works [*Tsyganenko and Usmanov*, 1984, *Tsyganenko*, 1988; 1990; 1991]. In the last of the above papers a quantitative model of the region 1 current circuit was proposed, based on a transformation of the magnetic vector potential of a cone-shaped electric current sheet. The method provided a reasonable representation for the contribution from the most large-scale higher-latitude Birkeland current system. However, that approach cannot be extended to lower-latitude region 2 field-aligned currents associated with the partial ring current system.

In the present work as well as in the companion paper by Stern [this issue] an attempt is made to bridge this gap. In contrast to the case of the region 1 system, there exists a clearer understanding of region 2 currents and a quantitative description of the basic physical mechanisms which give rise to them [*Vasyliunas*, 1970]. A simplifying assumption is that the background magnetic field in the region 2 domain does not deviate significantly from the dipolar configuration (which is equivalent to assuming that plasma beta is not too large) and hence the electric currents can be easily evaluated from data on the magnetospheric plasma distribution. This means that, in principle, the problem of determination of the magnetic field can be solved in a straightforward way by calculating Biot-Savart integrals over the region 2/partial ring current system.

However, this is only the first (and the easiest) part of the job: what we need for practical modeling of the magnetosphere and geomagnetic field line mapping is a set of simple analytical expansions yielding a convenient approximation for the numerically computed magnetic field components. Because of the complicated geometry of the partial ring current system [*Roelof*, 1989], the development of a global analytical B field model meets some difficulties. One possible solution to the problem is proposed below. Another approach based on formal transformations of the initially purely dipolar magnetic field is developed by Stern [this issue]. In spite of basic difference in starting points (plasma pressure distribution in the present work and modified Euler potentials in that of Stern) and mathematical treatment (a direct analytical fitting of **B** components in this work and "shifted" spherical harmonic expansions for the scalar potential in the companion paper), the results are much similar, at least qualitatively.

2. MAGNETIC FIELD DISTURBANCE PRODUCED BY THE PARTIAL RING CURRENT SYSTEM AND ITS NUMERICAL CALCULATION

The region 2 Birkeland current system (including the partial ring current) is believed to arise from an axially asymmetric intrusion of hot plasma into the near magnetosphere during disturbed periods. Some of the most striking evidence for such an asymmetric injection was presented by *Roelof* [1987] who showed by using the measurements of energetic neutral atoms that the night-day asymmetry in the ring current particle flux can rise to as high as 20:1 during storm time. *Iijima et al.* [1990], using AMPTE/CCE magnetometer data, found a midnight-noon asymmetry in the azimuthal electric current magnitude of the order of 3:1. Since the net volume current density should be divergenceless, the local time asymmetry of the cross-B current gives rise to Birkeland current j_B, whose density can be evaluated from the equation $\nabla \cdot j = 0$.

$$\frac{\partial}{\partial s}\left(\frac{j_B}{B_0}\right) = \frac{2c(\mathbf{B}_0 \times \nabla B_0) \cdot \nabla p}{B_0^4} \quad (1)$$

where, for the sake of simplicity, the plasma pressure is

assumed to be isotropic, and the coordinate s along the magnetic field line is measured from the northern ionosphere to the equator (that is, oppositely to the B_0 vector).

The next simplifying assumption is that the background magnetic field B_0 is purely dipolar, which can be justified by the relatively low latitude of the region 2 currents. In other words, we suppose a basic day-night asymmetry of the plasma pressure, while the corresponding magnetic field asymmetry is assumed to be negligible. This implies that the plasma beta parameter in the partial ring current region is not large. The last assumption becomes questionable for strongly disturbed periods, during which a significant inflation of the nightside magnetosphere at $L\sim6$-8 is observed due to injection of hot plasma. One more implication of the day-night asymmetry in the real magnetosphere is that the center of the region 2 quasi-circular zone does not coincide with the geomagnetic pole but is shifted to nightside by several degrees. The present model fails to take into account these features and should thus be considered as just a first step in developing an elaborate model of the partial ring current.

Let us introduce the coordinates

$$\alpha = \frac{\sin^2\theta}{r} = r_e^{-1} \qquad (2)$$

$$\gamma = \frac{\cos\theta}{r^2} = r_p^{-2} \qquad (3)$$

The variables α, γ, and the azimuthal angle ϕ define an orthogonal coordinate system [*Stern*, 1976] in which the surfaces $\alpha =$ const are the dipolar L shells of radius r_e, while $\gamma =$ constant are surfaces of constant scalar potential and cross the polar axis at $r = r_p$. The inverse transformation from a pair of the coordinates (α,γ) to (r,θ) is more cumbersome (see Appendix A).

In the case of isotropic plasma the pressure p does not depend on γ, and we obtain from (1) the volume density of Birkeland current,

$$j_B = \frac{6c\sqrt{1 + 3\cos^2\theta}}{\alpha^2 M \sin^6\theta} I(\cos\theta) \frac{\partial p}{\partial \phi} \qquad (4)$$

where M is the Earth's dipole moment and

$$I(x) = \frac{1}{243}\left(\frac{27}{7}x^7 - \frac{99}{5}x^5 + \frac{117}{3}x - 13x + \frac{256x}{1 + 3x^2}\right) \qquad (5)$$

It can be seen from (4) that the field-aligned current is proportional to the azimuthal component of the pressure gradient which is positive (negative) in the dusk (dawn) sector of northern hemisphere and hence j_B is positive (negative) there, in accordance with the observed polarity of the region 2 currents.

Let us proceed now to the cross-B component of the current and its magnetic effect. It is convenient to treat separately contributions from the drift and magnetization part of the net current. The drift current density

$$J_d = \frac{2cp(\alpha,\phi)}{B_0^3} B_0 \times \nabla B_0 \qquad (6)$$

in the axially symmetric dipolar magnetic field B_0 has only the azimuthal component

$$j_{d\phi} = -\frac{6c \sin^5\theta (1 + \cos^2\theta)}{\alpha^2 M (1 + 3\cos^2\theta)^2} p(\alpha,\phi) \qquad (7)$$

Field-aligned and drift current contributions to the magnetic field can be found from (4)-(7) by evaluating the Biot-Savart integral

$$B_{B+d} = \frac{1}{c}\int\frac{(J_B + J_d)\times(r - r')}{|r - r'|^3}dv \qquad (8)$$

The magnetization current j_m, in contrast with j_d and j_B, contains the α component $\partial p/\partial\alpha$ of the pressure gradient. For this reason it is more convenient to replace the part of the Biot-Savart integral containing j_m by an equivalent presentation in which the current-carrying region is considered as a magnetized medium, with the function

$$\mu(r) = -\frac{p}{B_0^2} B_0 \qquad (9)$$

yielding the spatial distribution of the magnetization vector. The corresponding contribution to the magnetic field disturbance outside the current-carrying layer is given by

$$B_m(r) = \int\left[(r-r')\frac{3\mu \cdot (r')\cdot(r-r')}{|r-r'|^5} - \frac{\mu(r')}{|r-r'|^3}\right]dv \qquad (10)$$

where the integration is carried out with respect to r' over the space occupied by the partial ring current plasma.

The integral (10) is equivalent to the Biot-Savart one containing the diamagnetic current $j_m = c(\nabla\times\mu)$ in the integrand, but in contrast to the latter, does not include transverse derivatives of the plasma pressure. The principal advantage of the representation (10) is that it simplifies the calculation of the disturbance field if the region 2/partial ring current system is assumed to be distributed over a relatively thin L shell. This assumption reduces the numerical computation of the net disturbance field to a two-dimensional integration over the current carrying surface. As shown below, in the analytical model of the numerically computed magnetic field, the abruptness of a two-dimensional current can be removed by means of a smooth interpolation of the B components across the integration surface.

The next simplification can be introduced by making a special choice of the local time variation of the plasma pressure. In the general case, the axially asymmetric pressure function $p(\alpha,\phi)$ gives rise to an essentially three-dimensional distribution of the disturbance magnetic field which needs separate numerical evaluation at each local time; attempts to devise analytical representation for such a general field, are, inevitably, difficult. An effective way out is to expand the azimuthal variation of $p(\alpha,\phi)$ in Fourier series, retaining, in the simplest case, the two leading terms

$$p(\alpha,\phi) \sim (p_0 + \Delta p \cos \phi) \delta(\alpha - \alpha_0). \qquad (11)$$

The delta function factor represents the thin-layer approximation described earlier, where $\alpha_0 = r_{e0}^{-1}$ defines the location of the current-carrying L shell and the bracketed factor in (11) defines the cosinusoidal azimuthal variation of the pressure function between the minimal value $p_0 - \Delta p$ at noon and the maximal one $p_0 + \Delta p$ at midnight. As follows from (4) to (7), in this case the Birkeland current density varies as sine ϕ, while the drift current can be formally split up into a sum of two terms, of which the first one corresponds to an axially symmetric ring current parametrized by p_0 and the second one, proportional to Δp and varying as $\cos \phi$, yields a pair of loops closing the field-aligned current via the noon and midnight sectors at low latitudes. This is illustrated in Figure 1 which shows the two components of the partial ring current system on the surface $\alpha = \alpha_0$ and the resultant pattern of the current flow lines given by the sum of $\mathbf{j}_d$ and $\mathbf{j}_B$.

It should be noted that the idea of representing the partial ring current as the sum of the axisymmetric part and the quadrupole two-loop system was suggested earlier by *Stern* [1989], who proposed to model the magnetic effects of the region 2 system by making a formal modification of the Euler

potentials. In that approach the quadrupole electric current configuration arises as a result of assuming a sinusoidal variation of the first-order correction terms in the Euler potential expansions. Here we arrive at the same representation in quite a different way, starting from the asymmetric distribution of the plasma pressure. Note also that the net configuration shown in Figure 1c is quite similar to the one obtained by *Roelof* [1989] from the energetic neutral atom data on the ring current ion pressure.

It turns out that the formal separation of the net current into the symmetric part (Figure 1a) and the quadrupole part (Figure 1b) largely simplifies the task of devising an analytical representation for the disturbance magnetic field. Namely, the field produced by the axisymmetric part of the current system shown in Figure 1a and denoted henceforth as $\mathbf{B}_S$ is also axially symmetric, while the components of the field $\mathbf{B}_q$ from the quadrupole part (Figure 1b), at any point of space however close to the current layer, include the azimuthal dependence only via the factor $\cos \phi$ or $\sin \phi$.

Specifically, the spherical components of $\mathbf{B}_q$ can be represented as

$$B_{qr}(r, \theta, \phi) = b_{qr}(r,\theta) \cos \phi$$
$$B_{q\theta}(r, \theta, \phi) = b_{q\theta}(r,\theta) \cos \phi \qquad (12)$$
$$B_{q\phi}(r, \theta, \phi) = b_{q\phi}(r,\theta) \sin \phi$$

Similarly, the components of the field from the magnetization current can also be divided into the dipolar (axisymmetric) and quadrupole terms. The validity of representation (12) was verified by direct numerical computation of the integrals (8) and (10); a mathematical proof is given in Appendix B.

Alternatively, instead of the r and θ components given by (12) we can introduce
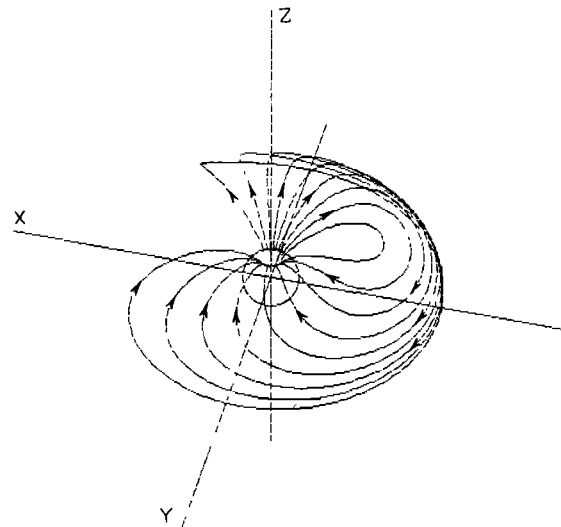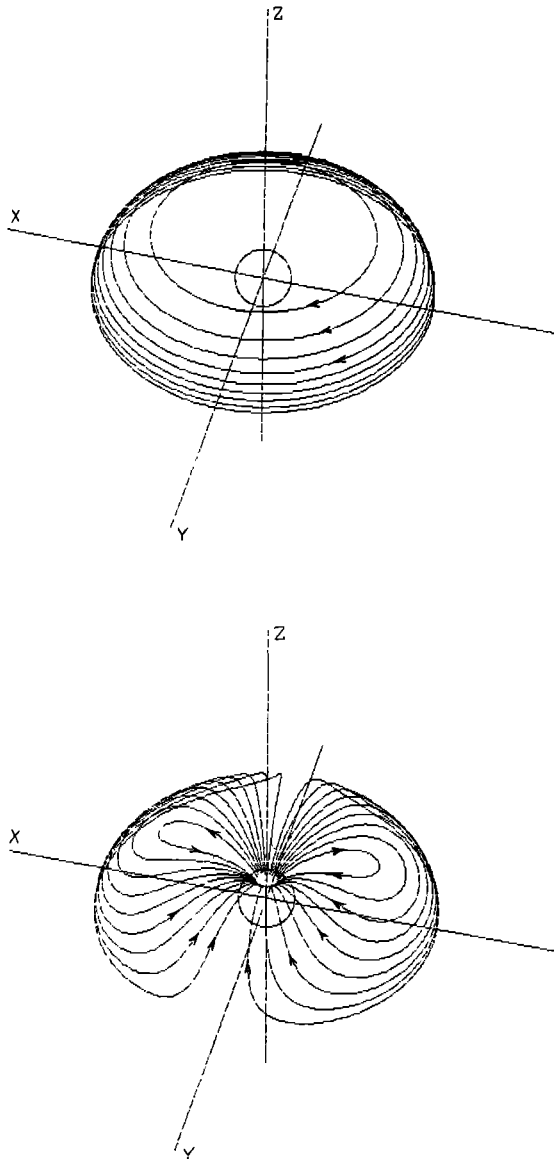

Fig. 1.Electric current flow lines in the model partial ring current computed from (4)-(7) on the surface $\alpha = \alpha_0$: (*a*) The axially symmetric ring current corresponding to the first term in (11). (*b*) The quadrupole part corresponding to the second term in (11) and containing Birkeland currents.(*c*) The resultant configuration given by the sum the systems (Figure 1a) and (Figure 1b). In this particular case $p_0 = \Delta p$ and therefore the electric current is zero in the noon meridian plane. The current flow lines of the southern hemisphere are not shown in the plots, all the patterns being symmetrical with respect to the equatorial plane.

$$B_\alpha = B_r v + B_\theta w$$

$$B_\gamma = B_\theta v - B_r w \; , \tag{13}$$

$$v = -\sin\theta / S$$

$$w = 2\cos\theta / S$$

$$S = \sqrt{1 + 3\cos^2\theta}$$

This choice proves to be more convenient than the spherical components (12), because everywhere on the L shell $\alpha = \alpha_0$ the B_α and B_γ components are normal and tangential, respectively, to the current layer. As a result, their distribution in α - γ space is much more orderly than that of B_r and B_θ.

3. ANALYTICAL REPRESENTATION OF THE NUMERICALLY COMPUTED MAGNETIC FIELD

Because of the separation of the azimuthal dependence of the magnetic field components as indicated in (12), the problem of analytical fitting is reduced, in fact, to two dimensions. What we have to do is to find convenient representations for the axisymmetric components $b_{s\alpha}(\alpha,\gamma)$ and $b_{s\gamma}(\alpha,\gamma)$ and the quadrupole ones $b_{q\alpha}(\alpha,\gamma)$, $b_{q\theta}(\alpha,\gamma)$.

In doing so, we meet the problem of satisfying the condition

$$\nabla \cdot \mathbf{B} = 0 \tag{14}$$

for the analytical $\mathbf{B}$ field. The original field given by integrals (8) and (10) is divergenceless and hence a violation of (14) can only be introduced by deficiencies of the analytical approximation. In principle, these difficulties could be avoided by deriving an appropriate analytical representation for the vector potential $\mathbf{A}$, which can also be numerically computed from the distributions of the electric current and magnetization vectors given by (6), (7), and (9). In such a case the analytical model magnetic field would be divergence-free by construction, since $\nabla \cdot (\nabla \times \mathbf{A})$ is identically zero. This approach was tried early in this work; however, it turned out that, as a rule, even an excellent approximation for $\mathbf{A}$ gave but a fair agreement for $\mathbf{B}$, while the electric current pattern showed only a gross resemblance to the expected distribution and included a number of spurious features. An obvious reason is that the $\mathbf{B}$ and $\mathbf{j}$ vectors are composed, respectively, of the first and second spatial derivatives of $\mathbf{A}$, so that a good fit for the latter does not guarantee as good approximations for the former ones.

As for the quadrupole part of the field, $\mathbf{B}_q$, there exists one more way to circumvent the problem of satisfying (14). Namely, because of the special kind of dependence of the $\mathbf{B}_q$ components on ϕ as given by (12), it is sufficient to fit only the first two components, while $\mathbf{B}_{q\phi}$ can be easily expressed in terms of $B_{q\alpha}$ and $B_{q\gamma}$ by applying and therefore identically satisfying equation (14). This approach implies, however, that the components of $\mathbf{j}$, again, contain dependence on the second derivatives of the approximation functions, which leads to the same difficulties.

Bearing all this in mind, it was finally decided to develop independent analytical approximations for all three components of the disturbance field. As shown below, due to the

good accuracy of the approximations, the divergence of the model field does not deviate significantly from zero.

As a starting point for constructing the analytical model, distributions of the magnetic field components ($B_{q\alpha}$, $B_{q\gamma}$, $B_{q\phi}$) for the quadrupole term and ($B_{s\alpha}$, $B_{s\gamma}$) for the axisymmetric term were found by numerically calculating the integrals (8) and (10) at 650 points of the (α-γ) space to provide a good coverage of the near-Earth region up to large geocentric distances. More specifically, the modeling region was divided into the inner part with $\alpha > \alpha_0$, lying inside the shell $r_e = 6$ R_E, and the outer part with $\alpha < \alpha_0$ extending up to $r_e = 700\, R_E$. A non-uniform grid in α-γ space was introduced, comprising 25 values of α (9 and 16 values in the inner and outer regions, respectively) and 26 values of γ corresponding to the interval $1 < r_p < 350\, R_E$. Due to the axial symmetry of the term $\mathbf{B}_s$ and the relations (12) for $\mathbf{B}_q$, the distribution of the field in the whole modeling region was obtained by computing the integrals for a single value of ϕ.

The integration was done over the two-dimensional surface $\alpha = \alpha_0$, according to the adopted thin-layer approximation (11), and the normalization factor in the integrand was chosen so that the net electric current flowing in the infinitely thin sheet was equivalent to that produced by an isotropic plasma population with $p = \Delta p = 20$ keV/cm^{-3} trapped within the interval $5.5\; R_E < r_e < 6.5\; R_E$. As can be verified by integrating (7) at the ionospheric level, this corresponds to a net (downward at dusk or upward at dawn) Birkeland current of about 260 kA.

3.1. Approximation for the Quadrupole Term

The distribution of the component b_{qa} (α,γ) is given in Figure 2, showing families of plots of $b_{q\alpha}$ against γ for the 25 values of α. The general shape of the profiles is the same both in the inner (Figure 2a) and outer (Figure 2b) regions, which allows one to represent them with the same functional form. A search for an appropriate function has led to the following:

$$b_{q\alpha}\,(\alpha,\gamma) = f_1(\alpha) \sin\gamma + f_2(\alpha) \frac{\gamma}{\sqrt{\gamma^2 + \gamma_1^2(\alpha)}} \tag{15}$$

A least squares fitting of the parameters f_1, f_2, and γ_1 for each of the curves in Figure 2 yielded their numerical values for the 25 values of α shown in Figures 3a- 3c by dots. All the profiles have distinct kinks between the inner and outer regions at the current-carrying boundary $\alpha = \alpha_0 = 0.167$. In order to simulate the finite thickness of the current layer in the α coordinate and to ensure a smooth matching between the inner and outer slopes of the approximating function, it is reasonable to ignore the points lying in the vicinity of the kink. The following analytical representations were chosen for f_1, f_2, and γ_1:

$$f_1(\alpha) = f_{10} + \sum_{i=1}^{3} f_{1i} \frac{\alpha - \alpha_{f1i}}{\sqrt{(\alpha - \alpha_{f1i})^2 + \Delta\alpha_{f1i}^2}} \tag{16}$$
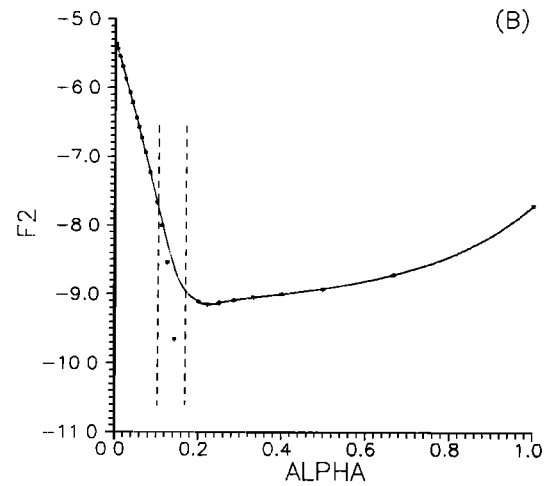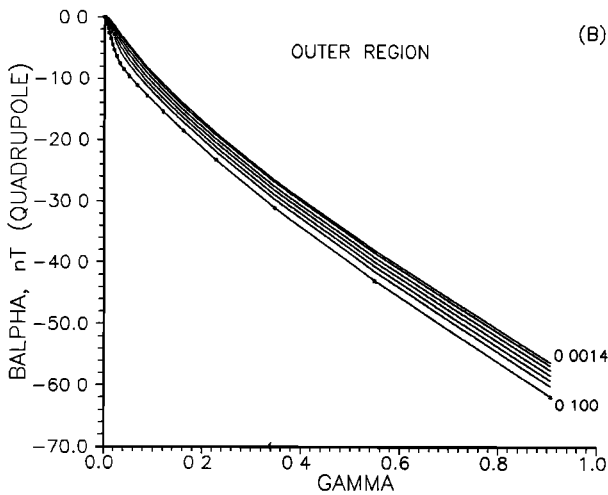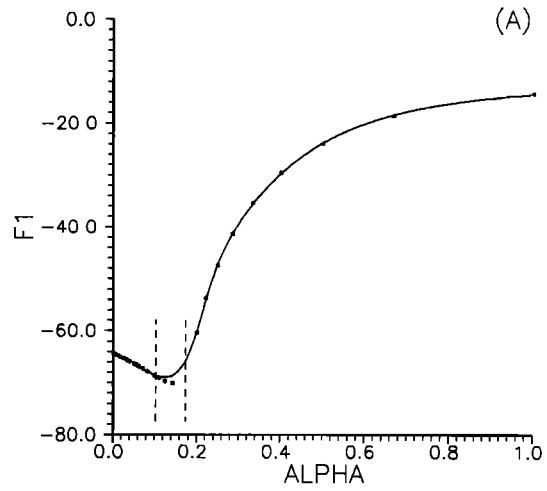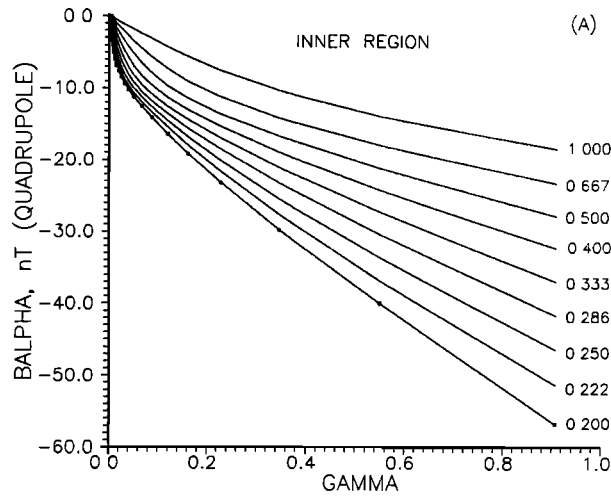
Fig. 2. The family of plots of the quadrupole component $b_{q\alpha}$ against γ computed for a set of 25 values of the α coordinate: (a) Plots for the inner region $\alpha > \alpha_0$ ($r_e < r_{eo}$), (b) Plots for the outer region $\alpha < \alpha_0$ ($r_e > r_{eo}$). The curves are labeled by the corresponding values of α; in the plot (Figure 2b) only the marginal values are given. The disturbance magnetic field magnitude in this and all the foregoing figures corresponds to the net Birkeland current of about 260 kA per each hemisphere (see text).

$$f_2(\alpha) = f_{20} + f_{21}\xi + f_{22}\xi^2 + f_{23}\frac{1}{\sqrt{(\alpha - \alpha_{f23})^2 + \Delta\alpha_{f23}^2}}$$

$$+ f_{24}\frac{\alpha - \alpha_{f24}}{\sqrt{(\alpha - \alpha_{f24})^2 + \Delta\alpha_{f24}^2}}, \qquad (17)$$

where

$$\xi = 0.5\left[\sqrt{(\alpha - \alpha_{\xi f2})^2 + \Delta\alpha_{\xi f2}^2} - (\alpha - \alpha_{\xi f2})\right]$$

and

$$\gamma_1(\alpha) = \gamma_{10} + \gamma_{11}\xi^2 + \gamma_{12}\frac{\eta - \eta_{\gamma 1}}{\sqrt{(\eta - \eta_{\gamma 1})^2 + \Delta\eta_{\gamma 1}^2}}, \qquad (18)$$
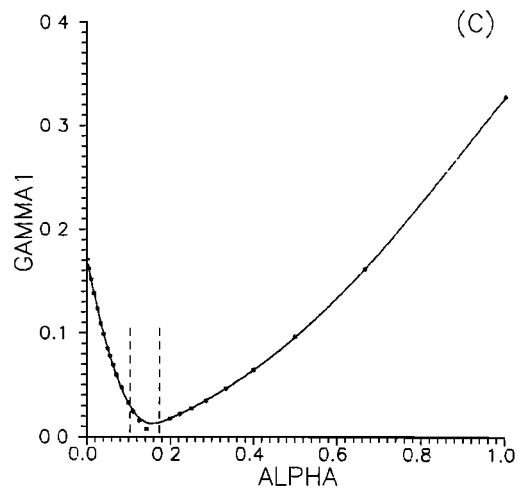
Fig. 3. The results of least squares fitting the $b_{q\alpha}$ plots of Figure 2 by the functions (15-18): (a)The dependence of the parameter f_1 on α; the dots correspond to the "first-level" fitting using (15) and the solid line gives the best fit approximation (16), (b) As in the Figure 3a, for the parameter f_2 approximated by (17). (c) As in the Figure 3a, for the parameter γ_1 approximated by (18). In each case the points lying between the dashed lines were ignored by the least squares procedure, which gave a smooth transition between the inner and outer slopes resulting in a distributed current layer.

where

$$\xi = 0.5\left[\sqrt{(\alpha-\alpha_{\xi\gamma1})^2 + \Delta\alpha_{\xi\gamma1}^2} - (\alpha-\alpha_{\xi\gamma1})\right]$$

$$\eta = \xi + (\alpha-\alpha_{\xi\gamma1})$$

The function $(\alpha-\alpha_j)/[(\alpha-\alpha_j)^2 + \Delta\alpha_j^2]^{1/2}$ plays an important role in this representation, and the pairs of variables ξ and η proved to be effective for approximating continuous smooth functions which have essentially different behavior on opposite sides of a transition point $\alpha = \alpha_0$. The first variable, ξ, is nearly zero for $\alpha > \alpha_0$ and varies linearly for $\alpha < \alpha_0$, while the second one, η, is the mirror reverse of ξ with respect to α_0. As a result, composing sums $f(\xi) + g(\xi)$ or, for a more general case with multiple transition points, $f(\xi_i+\eta_j) + g(\xi_j+\eta_k)$, enables one to develop analytical fits to a large variety of possible functions.

Solid lines in Figures 3a-3c show the analytical approximations (16-18) fitting the dotted profiles obtained by an iterative least squares procedure. In each case the three points corresponding to $r_e = 7.0$, 8.0, and 9.0 were ignored, which resulted in a smooth transition between the inner and outer current-free regions. Table 1 gives numerical values of all parameters appearing in (16) - (18) and in the subsequent expressions (19) - (40) which define the rest of the model.

Figure 4 presents distributions of the $b_{q\gamma}$ component in the same format as was used for $b_{q\alpha}$ in Figure 2. In this case there is a significant difference between the two families corres-

ponding to $\alpha > \alpha_0$ and $\alpha < \alpha_0$. The final functional form for representing $b_{q\gamma}$ was chosen as

$$b_{q\gamma}(\alpha,\gamma) = g_0(\beta) + g_1(\beta)\frac{\zeta}{\gamma^2 + \gamma_2^2(\beta)} \\ + g_2(\beta)\frac{1}{\sqrt{\gamma^2 + \gamma_2^2(\beta)}} \quad (19)$$

where $\zeta = \sqrt{\gamma^2 + d^2(\beta)}$. Here we have five parameters $(g_0, g_1, g_2, \gamma_2,$ and $d)$ depending on $\beta = \sqrt{\alpha}$, rather than on α; this choice of the argument is more convenient because, in line with symmetry considerations, $b_{q\gamma}$ shows a linear dependence on θ near the z axis. The following approximations for the parameters were adopted, namely

$$g_k(\beta) = \beta\left[g_{k0} + \sum_{i=1}^{3} g_{ki}\frac{\beta-\beta_{gki}}{\sqrt{(\beta-\beta_{gki})^2 + \Delta\beta_{gki}^2}}\right], \quad (20)$$

where $k = 0$, 1, and 2,

$$\gamma_2(\beta) = \gamma_{20} + \sum_{i=1}^{3} \gamma_{2i}\frac{\beta-\beta_{\gamma2i}}{\sqrt{(\beta-\beta_{\gamma2i})^2 + \Delta\beta_{\gamma2i}^2}}, \quad (21)$$

TABLE 1. Best Fit Values of the Model Partial Ring Current Parameters

Formula	Parameter Values*			
16	$f_{10} = -46.42$	$f_{11} = -122.8$	$f_{12} = 11.99$	$f_{13} = 145.9$
	$\alpha_{f11} = 0.09414$	$\Delta\alpha_{f11} = 0.2022$	$\alpha_{f12} = 0.2108$	$\Delta\alpha_{f12} = 0.05493$
	$\alpha_{f13} = 0.1141$	$\Delta\alpha_{f13} = 0.2620$		
17	$f_{20} = -4.849$	$f_{21} = 29.75$	$f_{22} = -27.99$	$f_{23} = -0.004782$
	$f_{24} = 4.519$	$\alpha_{f2} = 0.03^*$	$\Delta\alpha_{f2} = 0.1502$	$\alpha_{f23} = 0.220$
	$\Delta\alpha_{f23} = 0.0348$	$\alpha_{f24} = 1.321$	$\Delta\alpha_{f24} = 0.393$	
18	$\gamma_{10} = 0.2797$	$\gamma_{11} = 6.647$	$\gamma_{12} = 0.3778$	$\alpha_{\xi\gamma1} = 0.1551$
	$\Delta\alpha_{\xi\gamma1} = 0.03^*$	$\eta_{\gamma1} = 0.7494$	$\Delta\eta_{\gamma1} = 0.7276$	
20	$g_{00} = 2.093$	$g_{01} = 2.304$	$g_{02} = 4.305$	$g_{03} = -2.274$
	$\beta_{go1} = 0.6675$	$\Delta\beta_{go1} = 0.3863$	$\beta_{go2} = 0.3749$	$\Delta\beta_{go2} = 0.1304$
	$\beta_{go3} = 0.3791$	$\Delta\beta_{go3} = 0.07^*$		
	$g_{10} = -8.947$	$g_{11} = -8.730$	$g_{12} = 0.2307$	$g_{13} = 0.1629$
	$\beta_{g11} = 1.141$	$\Delta\beta_{g11} = 0.1165$	$\beta_{g12} = 0.2006$	$\Delta\beta_{g12} = 0.1821$
	$\beta_{g13} = 0.3749$	$\Delta\beta_{g13} = 0.06^*$		
	$g_{20} = 62.49$	$g_{21} = 63.10$	$g_{22} = -0.1730$	$g_{23} = 0.03397$
	$\beta_{g21} = 1.3609$	$\Delta\beta_{g21} = 0.1721$	$\beta_{g22} = 0.2065$	$\Delta\beta_{g22} = 0.08875$
	$\beta_{g23} = 0.6329$	$\Delta\beta_{g23} = 0.07^*$		
21	$\gamma_{20} = 4.796$	$\gamma_{21} = 4.851$	$\gamma_{22} = -0.05983$	$\gamma_{23} = -0.001735$
	$\beta_{\gamma21} = 1.316$	$\Delta\beta_{\gamma21} = 0.1806$	$\beta_{\gamma22} = 0.2785$	$\Delta\beta_{\gamma22} = 0.2238$
	$\beta_{\gamma23} = 0.6315$	$\Delta\beta_{\gamma23} = 0.1^*$		
22	$d_0 = 0.09164$	$d_1 = 0.007276$	$d_2 = -0.02285$	$d_3 = 0.09208$
	$\beta_d = 0.20^*$	$\Delta\beta_d = 0.02^*$	$\eta_d = 0.2826$	$\Delta\eta_d = 0.05532$

TABLE 1. (Continued)

| Formula	Parameter Values*		
24	$h_{10} = 9.125$ $h_{14} = 15.96$ $\Delta\alpha_{h12} = 0.09002$ $\Delta\alpha_{h14} = 0.6993$	$h_{11} = 32.57$ $\alpha_{h11} = 0.1103$ $\alpha_{h13} = 0.1442$	$h_{12} = 8019.$ $\Delta\alpha_{h11} = 0.03181$ $\Delta\alpha_{h13} = 0.08868$	$h_{13} = -8080.$ $\alpha_{h12} = 0.1442$ $\alpha_{h14} = 0.4497$
25	$h_{20} = 6.378$ $h_{24} = 23.96$ $\alpha_{h22} = 0.1994$ $\alpha_{h24} = 0.1211$	$h_{21} = 0.2826$ $\alpha_{h21} = 0.269$ $\Delta\alpha_{h22} = 0.00947$ $\Delta\alpha_{h24} = 0.03051$	$h_{22} = -0.5026$ $\alpha_w = 0.01331$ $\alpha_{h23} = 0.148$	$h_{23} = -28.88$ $\Delta\alpha_{h21} = 0.02433$ $\Delta\alpha_{h23} = 0.1733$
26	$h_{30} = -52.94$ $h_{34} = 102.7$ $\Delta\alpha_{h31} = 0.02*$	$h_{31} = -110.9$ $h_{35} = 4.436$ $\Delta\eta_{h34} = 0.03463$	$h_{32} = -15.39$ $\alpha_{h31} = 0.1707$ $\Delta\eta_{h35} = 1.003$	$h_{33} = 103.5$ $\alpha_w = 0.00175$
27	$\gamma_{30} = 0.5491$ $\Delta\alpha_{\gamma3} = 0.08581$	$\gamma_{31} = 10.59$ $\eta_{\gamma3} = 0.9916$	$\gamma_{32} = 0.7596$ $\Delta\eta_{\gamma3} = 1.059$	$\alpha_{\gamma3} = 0.1406$
29	$p_{00} = 4.485$ $p_{04} = 0.*$ $\Delta\gamma_{p03} = -0.003066$ $p_{13} = -0.02229$ $\Delta\gamma_{p12} = 0.0511$ $p_{22} = 0.1629$ $\Delta\gamma_{p21} = 0.008633$	$p_{01} = 0.05852$ $\Delta\gamma_{p0} = 0.003892$ $p_{10} = 0.09373$ $p_{14} = 0.*$ $\Delta\gamma_{p13} = 0.1194$ $p_{23} = 7.193\text{E-}5$ $\Delta\gamma_{p22} = 0.02737$	$p_{02} = 0.7067$ $\Delta\gamma_{p01} = 0.0046$ $p_{11} = -3.369$ $\Delta\gamma_{p1} = 0.0612$ $p_{20} = -8.333$ $p_{24} = 3.008$ $\Delta\gamma_{p23} = 0.02577$	$p_{03} = -0.003066$ $\Delta\gamma_{p02} = 0.02842$ $p_{12} = 3.849$ $\Delta\gamma_{p11} = 0.00915$ $p_{21} = -0.2815$ $\Delta\gamma_{p2} = 0.003324$
30	$p_{30} = 0.04043$ $p_{34} = -2.555\text{E-}6$ $\Delta\gamma_{p33} = 9.600\text{E-}3$	$p_{31} = -0.07719$ $\Delta\gamma_{p3} = 1.146\text{E-}3$ $\Delta\gamma_{p34} = 0.0104$	$p_{32} = -0.01124$ $\Delta\gamma_{p31} = 5.978\text{E-}3$	$p_{33} = 3.241\text{E-}4$ $\Delta\gamma_{p32} = 9.141\text{E-}3$
31	$\Delta\xi_0 = 0.04375$ $\Delta\gamma_\xi = 0.1209$	$\Delta\xi_1 = 0.3747$ $\Delta\gamma_\zeta = 5.526\text{E-}5$	$\zeta_1 = 2.394\text{E-}3$	$\Delta\zeta_1 = 2.709\text{E-}3$
32	$\eta_{p20} = -0.0827$ $\Delta\zeta_{\eta p22} = 0.03203$	$\eta_{p21} = 0.1800$ $\Delta\zeta_{\eta p23} = 0.3818$	$\eta_{p22} = 0.2448$ $\Delta\gamma_\eta = 4.45\text{E-}3$	$\eta_{p23} = 0.4616$
33	$\Delta\eta_{p20} = 0.08208$ $\Delta\zeta_{\Delta\eta p22} = 0.01754$	$\Delta\eta_{p21} = 0.1128$ $\Delta\zeta_{\Delta\eta p23} = 0.3070$	$\Delta\eta_{p22} = 0.1088$ $\Delta\gamma_{\Delta\eta} = 7.123\text{E-}4$	$\Delta\eta_{p23} = 0.3286$
35	$q_{00} = 1.287$ $q_{04} = 6.344\text{E-}3$ $\Delta\zeta_{q01} = 2.888\text{E-}3$ $\Delta\zeta_{q03} = 0.2000$ $\Delta\zeta_{q05} = 0.01884$	$q_{01} = -0.8869$ $q_{05} = 6.67\text{E-}2$ $\zeta_{q02} = 0.01239$ $\zeta_{q04} = 0.01028$ $\gamma_{q0} = 5.199\text{E-}5$	$q_{02} = 1.221$ $q_{06} = 0.442$ $\Delta\zeta_{q02} = 8.016\text{E-}3$ $\Delta\zeta_{q04} = 6.034\text{E-}3$	$q_{03} = -0.3252$ $\zeta_{q01} = 2.002\text{E-}3$ $\zeta_{q03} = 0.3217$ $\zeta_{q05} = 0.04327$
36	$q_{10} = -10.07$ $q_{14} = -4.674$ $\zeta_{q12} = 0.01924$ $\zeta_{q14} = 0.09675$	$q_{11} = 10.19$ $\zeta_{q11} = 0.0*$ $\Delta\zeta_{q12} = 0.01438$ $\Delta\zeta_{q14} = 0.01525$	$q_{12} = -5.232$ $\Delta\zeta_{q11} = 4.426\text{E-}3$ $\zeta_{q13} = 0.03555$ $\gamma_{q1} = 1.262\text{E-}3$	$q_{13} = 1.846$ $\Delta\xi_{q13} = 0.0671$
37	$q_{20} = -32.78$ $q_{24} = 3.058$ $\Delta\zeta_{q22} = 0.03066$ $\Delta\zeta_{q24} = 0.2284$	$q_{21} = -27.67$ $\zeta_{q21} = 0.03281$ $\zeta_{q23} = 3.309\text{E-}4$ $\gamma_{q2} = 1.0\text{E-}5*$	$q_{22} = 64.90$ $\Delta\zeta_{q21} = 0.01606$ $\Delta\zeta_{q23} = 0.01339$	$q_{23} = 0.00598$ $\zeta_{q22} = 0.03213$ $\zeta_{q24} = 0.1029$
38	$q_{30} = -0.01069$ $q_{34} = -0.1142$ $\zeta_{q32} = 0.0359$ $\xi_{q3} = 0.09608$ $\Delta\zeta_\xi = 0.01*$	$q_{31} = -0.03202$ $q_{35} = -7.0\text{E-}6$ $\Delta\zeta_{q32} = 0.01305$ $\Delta\xi_{q3} = 0.06922$ $\gamma_{q3} = 5.0\text{E-}4*$	$q_{32} = 0.0237$ $\zeta_{q31} = 0.2931$ $\zeta_{q33} = 0.04509$ $\Delta\zeta_{q35} = 2.221\text{E-}3$	$q_{33} = -0.1002$ $\Delta\zeta_{q31} = 0.06616$ $\Delta\zeta_{q33} = 0.05109$ $\zeta_\xi = 0.1511$
39	$\alpha_{00} = -0.1381$ $\Delta\zeta_{\alpha01} = 0.082$ $\Delta\zeta_{\alpha03} = 0.36$	$\alpha_{01} = 9.942$ $\zeta_{\alpha02} = 0.039$ $\gamma_{\alpha0} = 0.003*$	$\alpha_{02} = 0.3151$ $\Delta\zeta_{\alpha02} = 0.046$	$\alpha_{03} = 0.4775$ $\zeta_{\alpha03} = 0.265$
40	$\eta_{10} = -0.1827$ $\Delta\zeta_{\eta12} = 0.021$	$\eta_{11} = 0.9298$ $\gamma_{\eta1} = 0.0149$	$\eta_{12} = 0.2471$	$\Delta\zeta_{\eta11} = 0.2885$

*Fixed ones are denoted by asterisks.
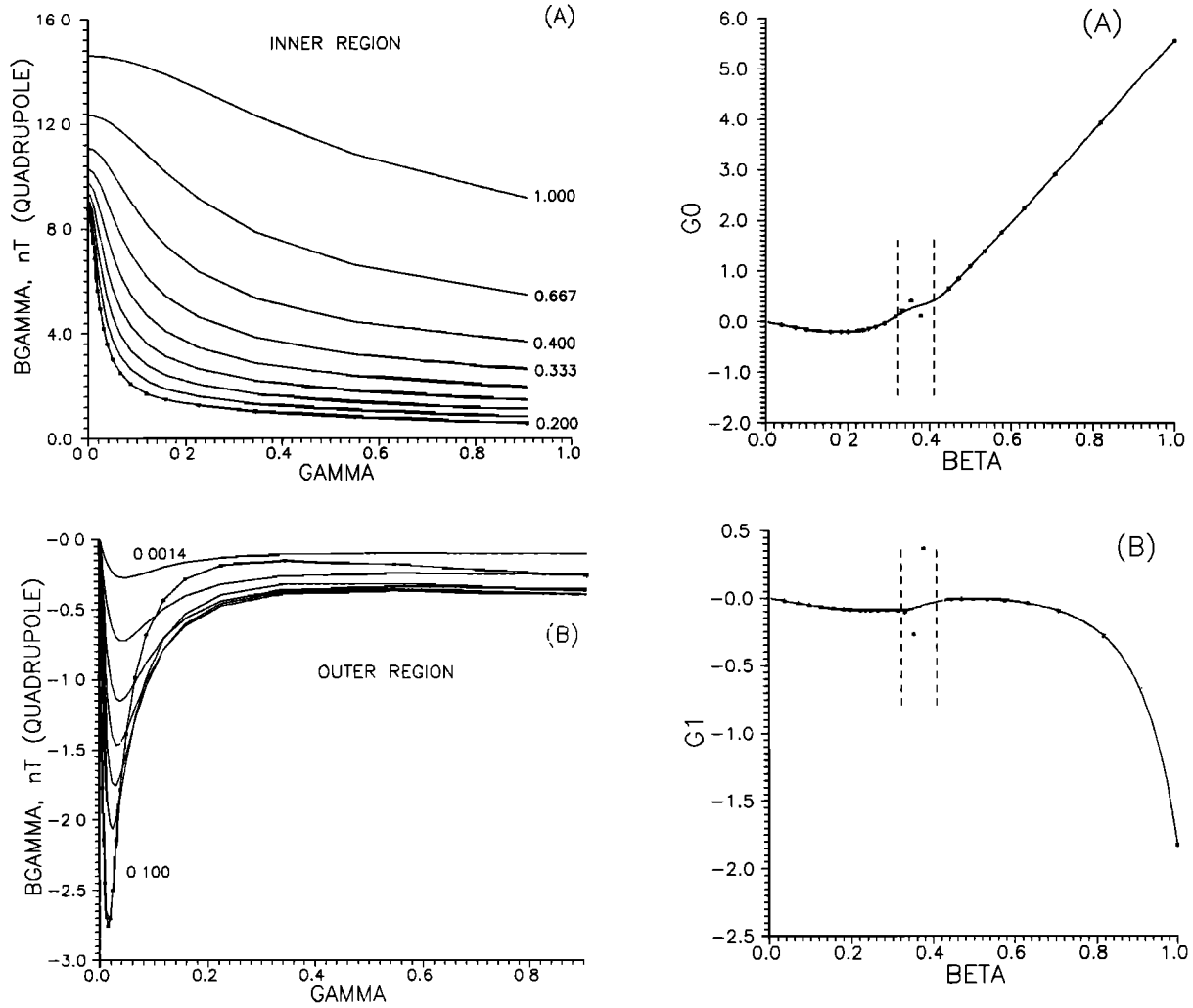
Fig. 4. The family of plots of the quadrupole component $b_{q\gamma}$ against γ computed for a set of 25 values of the α coordinate: (a) Plots for the inner region $\alpha > \alpha_0$ ($r_e < r_{e0}$), (b) Plots for the outer region $\alpha < \alpha_0$ ($r_e > r_{e0}$). The curves are labeled by the corresponding values of α; in Figure 4b only the marginal values are given.

$$d(\beta) = d_0 + d_1\xi + d_2\xi^2 + d_3\frac{\eta-\eta_d}{\sqrt{(\eta-\eta_d)^2 + \Delta\eta_d^2}} \quad (22)$$

where $\xi = 0.5\left[\sqrt{(\beta-\beta_d)^2 + \Delta\beta_d^2} - (\beta-\beta_d)\right]$ and where

$\eta = \xi + (\beta-\beta_d)$. The corresponding plots are given in Figure 5.

The azimuthal component distribution in the dawn-dusk meridian plane is presented by two families of $b_{q\phi}$ (α,γ) plots shown in Fig. 6. In this case the following analytical representation was chosen

$$b_{q\phi}(\alpha,\gamma) = \gamma\left[h_1(\alpha) + h_2(\alpha)\gamma^2 + h_3(\alpha)\frac{1}{\sqrt{\gamma^2+\gamma_3^2(\alpha)}}\right]$$
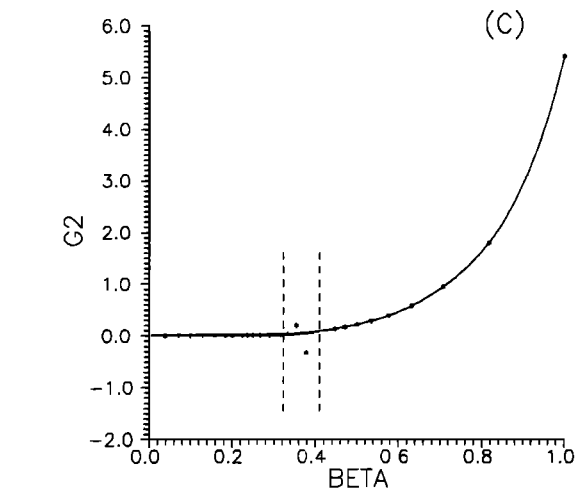
$$(23)$$

Fig. 5. The results of least squares fitting of the $b_{q\gamma}$ plots of Figure 4 by the functions (19)-(22): (a) The dependence of the parameter g_0 on β; the dots correspond to the "first-level" fitting by using (19) and the solid line gives the best-fit approximation (20), (b) Same as in Figure 5a, for the parameter g_1 approximated by (20). (c) Same as in Figure 5a, for the parameter g_2 approximated by (20). (d) Same as in the panel (a), for the parameter γ_2 approximated by (21). In each case, the points lying between the dashed lines were ignored by the least squares procedure, which gave a smooth transition between the inner and outer slopes resulting in a distributed current layer.
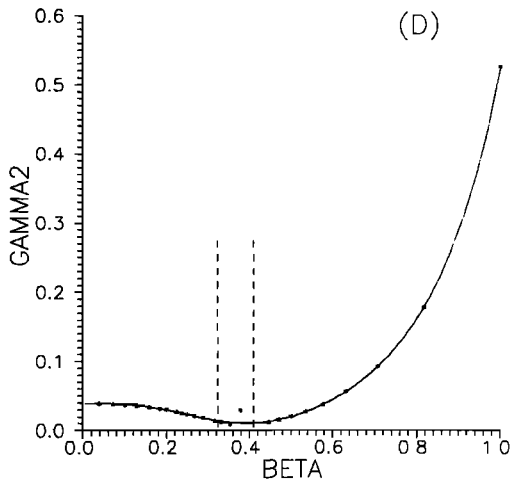
Fig. 5. (continued)

with

$$h_1(\alpha) = h_{10} + \sum_{i=1}^{4} h_{1i} \frac{\alpha - \alpha_{h1i}}{\sqrt{(\alpha - \alpha_{h1i})^2 + \Delta\alpha_{h1i}^2}}, \quad (24)$$

$$h_2(\alpha) = h_{20} + h_{21} \left[\frac{\alpha - \alpha_{h21} + \alpha_w}{\sqrt{(\alpha - \alpha_{h21} + \alpha_w)^2 + \Delta\alpha_{h21}^2}} \right.$$

$$- \frac{\alpha - \alpha_{h21} - \alpha_w}{\sqrt{(\alpha - \alpha_{h21} - \alpha_w)^2 + \Delta\alpha_{h21}^2}} \right]$$

$$+ h_{22} \frac{1}{\sqrt{(\alpha - \alpha_{h22})^2 + \Delta\alpha_{h22}^2}}$$

$$+ \sum_{i=3}^{4} h_{2i} \frac{\alpha - \alpha_{h2i}}{\sqrt{(\alpha - \alpha_{h2i})^2 + \Delta\alpha_{h2i}^2}}. \quad (25)$$

$$h_3(\alpha) = h_{30} + h_{31}(\alpha - \alpha_{h31} / \left[\sqrt{(\alpha - \alpha_{h31} + \alpha_{w3})^2 + \Delta\alpha_{h31}^2} \right.$$

$$+ \left. \sqrt{(\alpha - \alpha_{h31} - \alpha_{w3})^2 + \Delta\alpha_{h31}^2} \right] + h_{32}\xi + h_{33}\xi^2$$

$$+ h_{34} \frac{\eta}{\sqrt{\eta^2 + \Delta\eta_{h34}^2}} + h_{35} \frac{\eta}{\sqrt{\eta^2 + \Delta\eta_{h35}^2}}, \quad (26)$$

where

$$\xi = \sqrt{(\alpha - \alpha_{h31} + \alpha_{w3})^2 + \Delta\alpha_{h31}^2} - (\alpha - \alpha_{h31} + \alpha_{w3}),$$

$$\eta = \sqrt{(\alpha - \alpha_{h31} - \alpha_{w3})^2 + \Delta\alpha_{h31}^2} + (\alpha - \alpha_{h31} - \alpha_{w3}),$$

and with

$$\gamma_3(\alpha) = \gamma_{30} + \gamma_{31}\xi^2 + \gamma_{32} \frac{\eta - \eta_{\gamma3}}{\sqrt{(\eta - \eta_{\gamma3})^2 + \Delta\eta_{\gamma3}^2}} \quad (27)$$

where

$$\xi = 0.5 \left[\sqrt{(\alpha - \alpha_{\gamma3})^2 + \Delta\alpha_{\gamma3}^2} - (\alpha - \alpha_{\gamma3}) \right]$$

$$\eta = \xi + (\alpha - \alpha_{\gamma3}).$$

3.2. Approximation for the Symmetric Ring Current Field

The magnetic field B_S produced by the axially symmetric part of the isotropic plasma distribution (11) was modeled by using, in general, the same approach as in the case of the
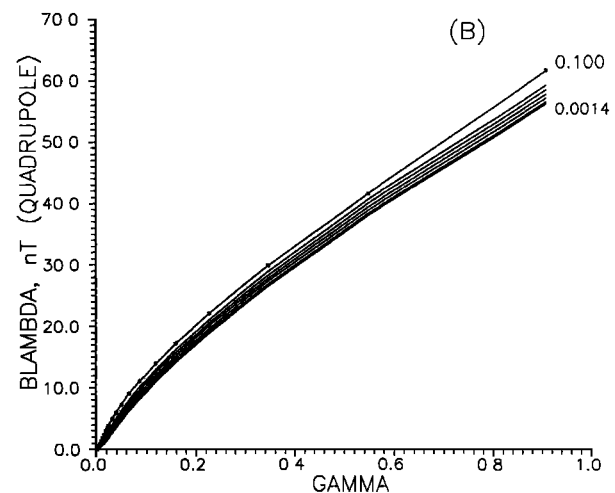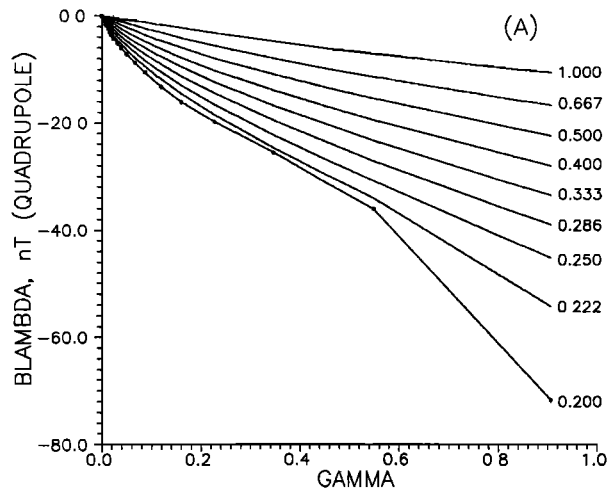

Fig. 6. The family of plots the quadrupole component $b_{q\gamma}$ against γ computed for a set of 25 values of the α coordinate: (a) Plots for the inner region $\alpha > \alpha_0$ ($r_e < r_{e0}$). (b) Plots for the outer region $\alpha < \alpha_0$ ($r_e > r_{e0}$). The curves are labeled by the corresponding values of α; in Figure 6b only the marginal values are given.

quadrupole term. However, in contrast with the latter, it was found easier to consider first the plots of $B_S(\alpha)$ for a selection of constant values of γ, that is to change the order of approximating the dependence on α and γ. Since $B_{S\alpha} \sim \beta = \sqrt{\alpha}$ for small α, it is convenient to start off with the family of plots of $f(\beta) = \beta^{-1} B_{S\alpha}(\beta)$ shown in Figure 7. For sufficiently large values of γ, the contours γ=const lie close to the Earth; that is why the plots for $\gamma \geq 0.1$ show a regular and almost monotone variation, while those with $\gamma \leq 0.1$ have sharp maxima at $\beta_0 = \sqrt{\alpha_0}$ corresponding to location of the ring current whose density at the low latitudes is much larger than in the near-Earth polar regions.

Attempts to find an appropriate functional form for $B_{S\alpha}$ resulted in the following one

$$B_{S\alpha} = \beta \left[p_0(\gamma) + p_1(\gamma) \frac{\xi}{\sqrt{\xi^2 + \Delta\xi^2(\gamma)}} \right.$$

$$+ p_2(\gamma) \frac{\eta - \eta_{p2}(\gamma)}{\sqrt{\left[\eta - \eta_{p2}(\gamma)\right]^2 + \Delta\eta_{p2}^2(\gamma)}}$$

$$\left. + p_3(\gamma) \frac{\beta - \beta_0}{\sqrt{(\beta - \beta_0)^2 + \Delta\beta_0^2}} \right], \qquad (28)$$

where

$$\xi = 0.5 \left\{ \sqrt{(\beta - \beta_0)^2 + \Delta\beta_0^2} - (\beta - \beta_0) \right\}$$

and

$$\eta = \xi + (\beta - \beta_0).$$

The second and third terms in curly brackets, respectively, approximate the left and right slopes of the profile shown in Figure 7, while the last term represents a jump at $\beta = \beta_0$ which is present on some curves.

The representation (28) contains four coefficients, $p_0...p_3$, and three nonlinear parameters, $\Delta\xi$, η_{p2}, and $\Delta\eta_{p2}$ which are functions of γ. The corresponding analytical fits were sought in the form

$$p_k(\gamma) = \frac{\gamma}{\sqrt{\gamma^2 + \Delta\gamma_{pk}^2}} \left[p_{k0} + \sum_{i=1}^{2} p_{ki} \frac{1}{\sqrt{\gamma^2 + \Delta\gamma_{pki}^2}} \right.$$

$$\left. + p_{k3} \frac{1}{\left(\gamma^2 + \Delta\gamma_{pk3}^2\right)^{3/2}} \right] + p_{k4}\gamma \qquad (29)$$

where k = 0, 1, and 2,

$$p_3(\gamma) = \frac{\gamma}{\sqrt{\gamma^2 + \Delta\gamma_{p3}^2}} \left[p_{30} + \sum_{i=1}^{4} p_{3i} \frac{1}{\left(\gamma^2 + \Delta\gamma_{p3i}^2\right)^{i/2}} \right], \qquad (30)$$
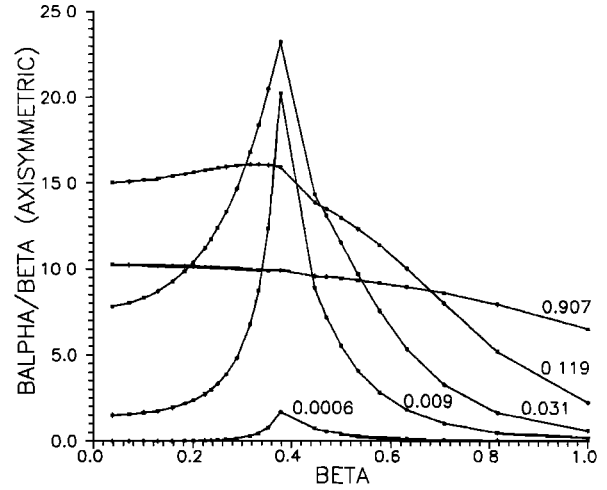

Fig. 7. Several plots showing the variation of $b_{S\alpha}\beta^{-1}$ for the axisymmetric model ring current along the contours of constant γ coordinate. The corresponding values of γ are given near the curves. The peaks at the plots for small values of γ are localized at the current layer position with $\beta = \beta_0 = \alpha_0^{1/2}$.

$$\Delta\xi(\gamma) = \Delta\xi_0 + \Delta\xi_1 \frac{\sqrt{(\zeta - \zeta_1)^2 + \Delta\zeta_1^2}}{\sqrt{\gamma^2 + \Delta\gamma_\xi^2}}, \qquad (31)$$

where $\zeta = \sqrt{\gamma^2 + \Delta\gamma_\zeta^2}$,

$$\eta_{p2}(\gamma) = \eta_{p20} + \eta_{p21}\zeta + \eta_{p22} \frac{\zeta}{\sqrt{\zeta^2 + \Delta\zeta_{\eta_{p22}}^2}}$$

$$+ \eta_{p23} \frac{\zeta}{\sqrt{\zeta^2 + \Delta\zeta_{\eta_{p23}}^2}} \qquad (32)$$

where $\zeta = \sqrt{\gamma^2 + \Delta\gamma_\eta^2}$, and

$$\Delta\eta_{p2}(\gamma) = \Delta\eta_{p20} + \Delta\eta_{p21}\zeta + \Delta\eta_{p22} \frac{\zeta}{\sqrt{\zeta^2 + \Delta\zeta_{\Delta\eta_{p22}}^2}}$$

$$+ \Delta\eta_{p23} \frac{\zeta}{\sqrt{\zeta^2 + \Delta\zeta_{\Delta\eta_{p23}}^2}} \qquad (33)$$

where $\zeta = \sqrt{\gamma^2 + \Delta\gamma_{\Delta\eta}^2}$.

At last, it only remains to give expressions for the $B_{S\gamma}$ component. Several typical profiles of $B_{S\gamma}$ distribution along

the lines of constant γ are shown in Figure 8. On going from larger to smaller values of γ, smooth profiles gradually pass into discontinuous ones with a jump at $\alpha = \alpha_0$.

Here again, the expression for the $B_{s\gamma}$-component was chosen as a sum of terms providing separate representation of the right and left branches of the curves. It was found that an accurate approximation can be obtained with the following functional form

$$B_{s\gamma}(\alpha,\gamma) = q_0(\gamma) + q_1(\gamma)\,\frac{\eta}{\sqrt{\eta^2+\eta_1^2(\gamma)}} + q_2(\gamma)\,\xi$$

$$+ q_3(\gamma)\left[\xi - \alpha_0(\gamma)\right]^3 \qquad (34)$$

where $\eta = 0.5\left\{\sqrt{\left[\alpha-\alpha_0(\gamma)\right]^2 + \Delta\alpha_0^2} + \left[\alpha-\alpha_0(\gamma)\right]\right\}$,

$$\xi = \eta - \left[\alpha-\alpha_0(\gamma)\right],$$

and $\Delta\alpha_0 = 0.02$.

Fitting (34) to the 26 numerically computed profiles of $B_{s\gamma}$ versus α yielded numerical values of the functions $q_0(\gamma)$, $q_1(\gamma)$, $q_2(\gamma)$, $q_3(\gamma)$, $\alpha_0(\gamma)$, and $\eta_1(\gamma)$, which, in turn were least squares fitted using the following

$$q_0(\gamma) = q_{00} + \sum_{i=1}^{3} q_{0i}\,\frac{\zeta-\zeta_{q0i}}{\sqrt{\left(\zeta-\zeta_{q0i}\right)^2 + \Delta\zeta_{q0i}^2}}$$

$$+ \sum_{i=4}^{5} q_{0i}\,\frac{1}{\sqrt{\left(\zeta-\zeta_{q0i}\right)^2 + \Delta\zeta_{q0i}^2}} + q_{06}\zeta^2 \qquad (35)$$
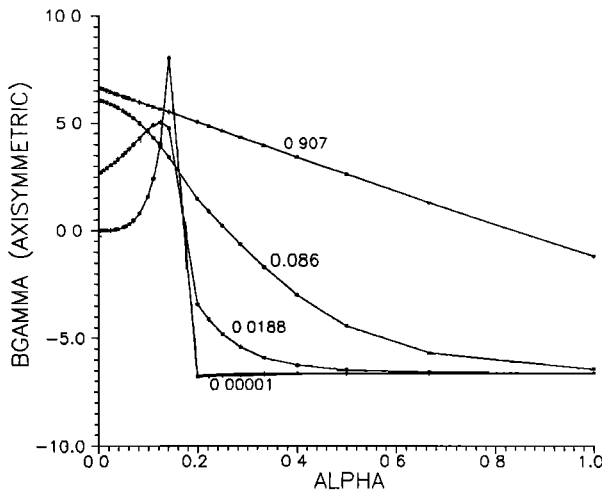

Fig. 8. Several plots showing the variation of $b_{s\gamma}$ for the axisymmetric model ring current along the contours of constant γ coordinate. The corresponding values of γ are given near the curves. The abrupt jumps at the plots for small values of γ are localized at the current layer position with $\alpha = \alpha_0$.

$$q_1(\gamma) = q_{10} + \sum_{i=1}^{2} q_{1i}\,\frac{\zeta-\zeta_{q1i}}{\sqrt{\left(\zeta-\zeta_{q1i}\right)^2 + \Delta\zeta_{q1i}^2}}$$

$$+ \sum_{i=3}^{4} q_{1i}\,\frac{1}{\sqrt{\left(\zeta-\zeta_{q1i}\right)^2 + \Delta\zeta_{q1i}^2}} \qquad (36)$$

$$q_2(\gamma) = q_{20} + \sum_{i=1}^{2} q_{2i}\,\frac{\zeta-\zeta_{q2i}}{\sqrt{\left(\zeta-\zeta_{q2i}\right)^2 + \Delta\zeta_{q2i}^2}}$$

$$+ q_{23}\,\frac{1}{\left(\zeta-\zeta_{q23}\right)^2 + \Delta\zeta_{q23}^2} +$$

$$+ q_{24}\,\frac{1}{\sqrt{\left(\zeta-\zeta_{q24}\right)^2 + \Delta\zeta_{q24}^2}}, \qquad (37)$$

$$q_3(\gamma) = \frac{1}{\left(\gamma^2+\gamma_{q3}^2\right)^2}\left[q_{30} + \sum_{i=1}^{3} q_{3i}\,\frac{\zeta-\zeta_{q3i}}{\sqrt{\left(\zeta-\zeta_{q3i}\right)^2 + \Delta\zeta_{q3i}^2}}\right.$$

$$+ q_{34}\,\frac{\xi-\xi_{q3}}{\sqrt{\left(\xi-\xi_{q3}\right)^2 + \Delta\xi_{q3}^2}} + q_{35}\,\frac{1}{\sqrt{\zeta^2 + \Delta\zeta_{q35}^2}}\left.\right], \qquad (38)$$

where, for $q_i(\gamma)$ in (35-38), $\zeta = \sqrt{\gamma^2+\gamma_{qi}^2}$, with $i = 0, 1, 2$, and 3, respectively, and

$$\xi = 0.5\left[\sqrt{(\zeta-\zeta_\xi)^2 + \Delta\zeta_\xi^2} - (\zeta - \zeta_\xi)\right].$$

The non-linear parameters were approximated as

$$\alpha_0(\gamma) = \alpha_{00} + \alpha_{01}\left(\sqrt{\zeta^2+\Delta\zeta_{\alpha01}^2} - \zeta\right)$$

$$+ \sum_{i=2}^{3} \alpha_{0i}\,\frac{\zeta - \zeta_{\alpha0i}}{\sqrt{\left(\zeta-\zeta_{\alpha0i}\right)^2 + \Delta\zeta_{\alpha0i}^2}} \qquad (39)$$

where

$$\zeta = \sqrt{\gamma^2+\gamma_{\alpha0}^2}$$

and

$$\eta_1(\gamma) = \eta_{10} + \sum_{i=1}^{2} \eta_{1i} \frac{\zeta}{\sqrt{\zeta^2 + \Delta\zeta^2_{\eta 1i}}}. \qquad (40)$$

where

$$\zeta = \sqrt{\gamma^2 + \gamma^2_{\eta 1}}.$$

4. RESULTS AND DISCUSSION

Table 1 summarizes the results of the least squares search for the model parameters entering in (15) - (40). The concrete forms of the above approximating functions including the number of terms, the initial values, and number of variable non-linear parameters were chosen in all cases according to individual features of the profiles to be fitted, in order to reach a compromise between the requirements of accuracy and simplicity of the model expressions. In most cases, the relative error of fitting the field components did not exceed a few tenths of percent throughout the whole current-free region $r_e \le 5\,R_E$ or $r_e \ge 10\,R_E$. The intermediate region is occupied by distributed currents spread out over the interval $r_e \le 5\,R_E$ or $r_e \ge 10\,R_E$, derived by the adopted procedure of smooth interpolation of the field components. This is illustrated by Figures 9-10 which show the transverse profiles of the electric current density in the partial ring current layer obtained by numerical calculation of the $\nabla\times B$ for the equatorial region and at high latitudes above the ionosphere. The plots correspond to the quadrupole part of the system which contains Birkeland currents. Figure 9 presents a near-equatorial profile of the azimuthal component of the $\nabla\times B$; it can be seen that the current attains the peak value at $r \approx 6\,R_E$ and gradually decreases on both sides from the maximum. The solid line without dots gives the variation of the disturbance magnetic field, and the dotted line shows distribution of $\nabla\cdot B$. As discussed in the beginning of section 3, the violation of $\nabla\cdot B = 0$
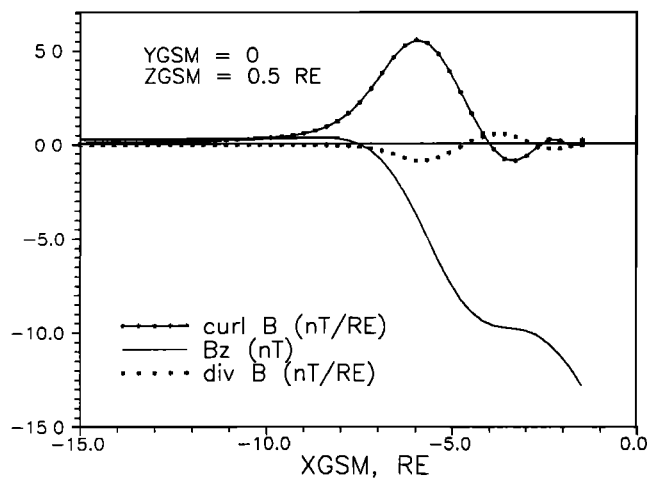

Fig. 9. Near-equatorial profiles of model B_z, $\nabla\times B$, and $\nabla\cdot B$, corresponding to the quadrupole part of the partial ring current system. The quantities are computed in the midnight meridian plane along the line $z = 0.5\,R_E$ parallel to the X_{GSM} axis.
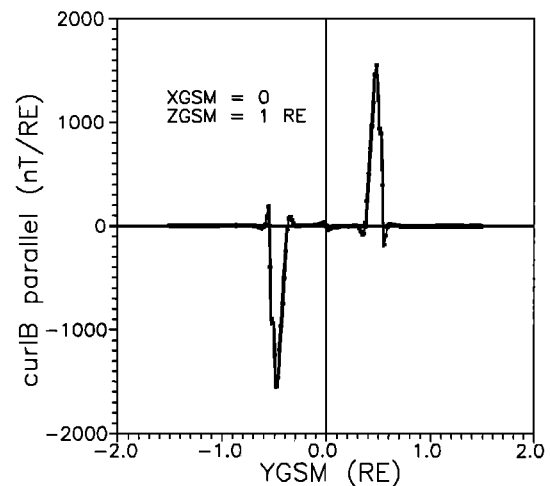

Fig. 10. A profile of the field-aligned component of $\nabla\times B$ yielding, within a constant factor, the model Birkeland current, computed along the line $z = 1\,R_E$ parallel to the Y_{GSM} axis and lying in the dawn-dusk meridian plane. Two layers of oppositely directed field-aligned currents are present at $Y \approx \pm 0.5\,R_E$. The small kink at $Y=0$ is an artifact of the numerical differentiation near the polar axis.

condition is due to the adopted independent representation of all three components of B. The relative importance of that unphysical feature can be tested by mapping a small square element in the equatorial plane to the ionosphere along the model field lines and evaluating the relative difference in the magnetic flux on both ends of the field line tube. The analytical field (15) - (40) calibrated to the net Birkeland current of 1 MA was added to the quiet magnetospheric field as given by the divergence-free model of Tsyganenko [1987] and a tracing procedure was carried out for a number of field line tubes. In most cases the relative difference in the magnetic flux did not exceed 10%, the largest values being observed within the interpolation region containing the current-carrying L shell.

Figure 10 corresponds to a dawn-dusk "polar pass" above the ionosphere and shows the profile of field-aligned component of $\nabla\times B$ computed at $z = 1\,R_E$ along the line $X_{GSM} = 0$ parallel to the Y_{GSM} axis. Note here that the model does not incorporate magnetic effects of the ionospheric electrojets which can be significant at low altitudes, but which rapidly fade out at larger distances and hence produce but a negligible effect on the pattern of field line mapping. Variation of the B_{XGSM} component of the disturbance field along the same line as in Figure 10 is shown in Figure 11. As can be expected, we have an almost constant antisunward field in the polar region, which abruptly becomes sunward on crossing the layers of Birkeland current and approaches zero at larger distance.

Figure 12 present the plots of $(\nabla\times B)_\phi$, B_{sz}, and $\nabla\cdot B_s$, corresponding to the axisymmetric part of the ring current, along the line y=0, z=0.5 R_E in the midnight meridian plane. Again, as a result of the smooth interpolation procedure, the original infinitely thin current surface is transformed into a spread-out distribution of the volume current density. The magnetic field variation reflects typical features of many ring current models: a depressed nearly uniform field at inner L shells and a rapidly decreasing dipolelike B_s outside the current-carrying region. As in the case of the quadrupole field, the magnitude of $\nabla\cdot B_s$, is also relatively small.
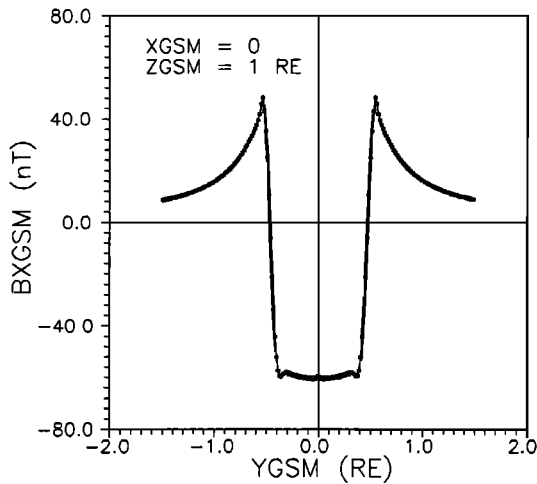
Fig. 11. Profile of the B_{XGSM} component of the magnetic field produced by the electric current distribution illustrated in the preceding Figure 10, along the same line. The field is antisunward and is almost constant in the high-latitude polar region; on crossing the layers of Birkeland current we observe the abrupt jumps of B_X and its gradual decrease to zero at larger distances.
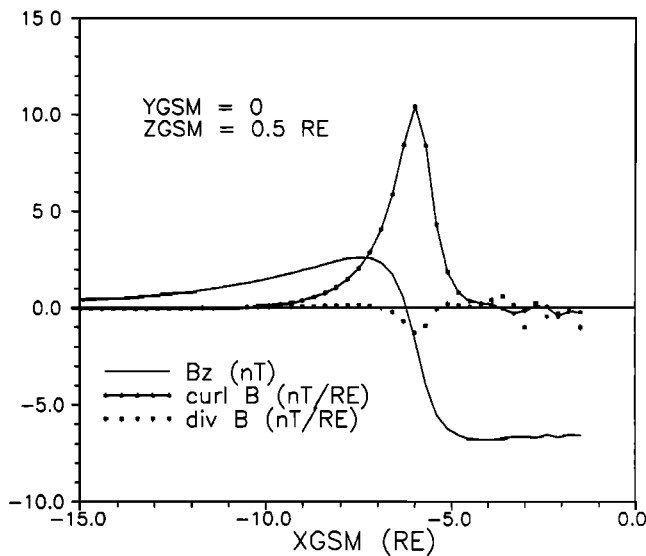

Fig. 12. Near-equatorial profiles of model B_z, $\nabla \times B$, and $\nabla \cdot B$, corresponding to the axisymmetric part of the partial ring current system. The quantities are computed in the midnight meridian plane along the line $z = 0.5\ R_E$ parallel to the X_{GSM} axis.

It should also be noted that, since the dipolar magnetic field is self-similar, the disturbance field produced by the model partial ring current can be easily scaled to any value of the characteristic distance $r_{e0} = \alpha^{-1}{}_0$. Namely, if "new" values of the net electric current and equatorial radius of the partial ring current are related to "old" ones as $I' = \chi I$ and $r'_{e0} = \nu r_{e0}$, then the corresponding "new" value of the disturbance field at a fixed point of space r can be evaluated as $B'(r) = (\chi/\nu)B(r/\nu)$. In empirical modeling of the magnetosphere based on sets of magnetometer data, the factors χ and ν should be considered as free parameters to be determined by a least squares fitting of the model to the measurements. One more degree of freedom can be introduced by allowing a rotation of the whole current

system by an angle ϕ_0 around the polar axis, simulating the local time shift of the partial ring current toward dusk sector deduced in early observations [e.g., *Kamide and Fukushima*, 1971] and modeled by *Usmanov and Tsyganenko* [1984].

In summary, a quantitative representation is developed for the magnetic field produced by a system with a partial ring current closed via large-scale region 2 Birkeland currents. The proposed analytical model is based on an electric current distribution consistent with the axially asymmetric distribution of hot isotropic plasma, the formation of which in the near magnetosphere is believed to be due to injections from the tail plasma sheet during substorms. The model contains four free parameters defining the net magnitudes of the electric current in the axially symmetric and quadrupole parts of the system, its characteristic scale size, and the angular position of the partial ring current with respect to midnight meridian.

The question of primary interest in implementing the above results for practical modeling of the magnetosphere is to determine to what extent does the partial ring current system affect the mapping the geomagnetic field lines. An answer to this question can be obtained by incorporating the representation (15) - (40) into a global model which correctly takes into account all other field sources including region 1 system of Birkeland currents, and then fitting that model to spacecraft data. This problem extends beyond the scope of the present paper and will be addressed in future works.

APPENDIX A: TRANSFORMATION FROM DIPOLAR TO SPHERICAL COORDINATES

From (2) and (3) we obtain the fourth-order equation for r

$$r^4 + \alpha\gamma^{-2} - \gamma^{-2} = 0 \qquad (A1)$$

Using the Descartes-Euler solution (*Korn and Korn*, 1968) and selecting a proper combination of signs, we arrive at the following expression for r in terms of α and γ

$$r = 4\left[\left(\sqrt{2g \cdot c} + \sqrt{c}\right)(g + c)\right]^{-1} \qquad (A2)$$

where

$$c = \left(\alpha^2/2 + \sqrt{f}\right)^{1/3} - \frac{4}{3}\left(\frac{\gamma^2}{\sqrt{f} + \alpha^2/2}\right)^{1/3}$$

$$f = \frac{64}{27}\gamma^2 + \frac{\alpha^4}{4}$$

$$g = \sqrt{c^2 + 4|\gamma|^{2/3}}$$

Substituting (A2) in (3), we obtain the necessary expression for θ.

APPENDIX B: ON SEPARATING THE AZIMUTHAL DEPENDENCE IN THE DISTURBANCE MAGNETIC FIELD COMPONENTS

The possibility of separating the dependence on ϕ in the components of B_q as given in (12), can be verified by representing the quadrupole term as

$$B_q = \nabla \times A_q, \qquad (B1)$$

where

$$A_q = \frac{1}{c} \int \frac{\mathbf{j}_q(\mathbf{r}')}{|\mathbf{r} - \mathbf{r}'|} dv, \qquad (B2)$$

with $\mathbf{j}_q$ corresponding to the quadrupole part of the divergenceless current $\mathbf{j}_d + \mathbf{j}_B$ containing the parameter Δp as the amplitude factor.

Let us assume first that the geocentric distance of the observation point r is larger than $r_{eo} = \alpha_0^{-1}$ or, in other words, the whole electric current system lies inside the sphere of radius r. In such a case the factor $|\mathbf{r} - \mathbf{r}'|^{-1}$ in the integrand can be expanded [e.g., *Korn and Korn*, 1968] as

$$|\mathbf{r} - \mathbf{r}'|^{-1} = \frac{1}{r} \sum_{n=0}^{\infty} \left(\frac{r'}{r}\right)^n \frac{(n-m)!}{(n+m)!}$$

$$\times c_m P_n^m(\cos\theta) P_n^m(\cos\theta') \cos m(\phi - \phi') \qquad (B3)$$

where $c_m = 1$ for $m = 0$ and $c_m = 2$ for $m > 0$.

The components of $\mathbf{j}_q$ contain factors $\sin \phi'$ or $\cos \phi'$, which can be rewritten as

$$\cos \phi \sin (\phi-\phi') + \sin \phi \cos (\phi-\phi')$$

and

$$\cos \phi \cos (\phi-\phi') - \sin \phi \sin (\phi-\phi') ,$$

respectively. Integrands corresponding to spherical components of the vector potential (B2) include scalar products of unit vectors $\mathbf{e}_r$, $\mathbf{e}_\theta$, $\mathbf{e}_\phi$ and $\mathbf{e}'_r$, $\mathbf{e}'_\theta$, $\mathbf{e}'_\phi$ in various combinations; these will also yield terms containing $\cos(\phi-\phi')$ and $\sin(\phi-\phi')$.

Because of the orthogonality of the sine and cosine functions, only a few terms of the expansion (B3) will provide a non zero contribution to (B2). By writing down explicitly the integrands for each component of A_q, it is easy to verify that

$$A_{qr} = a_{qr} (r,\theta) \sin \phi,$$
$$A_{q\theta} = a_{q\theta}(r,\theta) \sin \phi,$$
$$A_{q\phi} = a_{q\phi} (r,\theta) \cos \phi,$$

from which the above representation for B_q follows.

In a more general situation a part of the current system may be located at $r' > r$. In this case its contribution to the integral (B2) must be considered separately and the expansion (B3) should be made in powers of (r/r'). The remaining part of the proof is similar to the one given above.

Obviously, this result can be generalized for the case of more complex azimuthal variation of the pressure function. The principal statement here is that there is a one-to-one correspondence between the Fourier expansion terms for the local time distribution of pressure and for the components of the disturbance magnetic field. In other words, any harmonic term in the expansion for p (α,ϕ) gives rise to only one term of the same order in the expansions for B components.

REFERENCES

Iijima, T., T. A. Potemra, and L. J. Zanetti, Large-scale characteristics of magnetospheric equatorial currents, *J. Geophys. Res., 95*, 991, 1990

Kamide, Y., and N. Fukushima, Analysis of magnetic storms with DR-indices for equatorial ring current field, *Rep. Ionos. Space Res. Jpn., 25*, 125, 1971

Korn, G. A., and T. M. Korn. *Mathematical Handbook for Scientists and Engineers*, McGraw-Hill, New York, 1968.

Roelof, E. C.,Energetic neutral atom image of a storm-time ring current, *Geophys. Res. Lett., 19*, 652, 1987

Stern, D. P., Representation of magnetic fields in space, *Rev. Geophys., 14*, 199, 1976

Stern, D.P., Modeling of Birkeland currents, *IAGA Bull 53*, 6th Scientific Assembly, Exeter, 1989, Pt. 3 (Div. II & III Abstracts), p. 429, Int. Assoc. of Geomagn. and Aeron., Paris, 1989.

Stern, D.P., A simple model of Birkeland currents, *J. Geophys. Res.*, this issue.

Tsyganenko, N.A., Global quantitative models of the geomagnetic field in the cislunar magnetosphere for different disturbance levels, *Planet.Space Sci., 35*, 1347, 1987.

Tsyganenko, N. A., A quantitative model of the system of magnetospheric field-aligned currents, *Geomagn. Aeron.* Engl. Transl., *28*, 331, 1988

Tsyganenko, N. A., Quantitative models of the magnetospheric magnetic field: Methods and results, *Space Sci. Res., 54*, 75, 1990.

Tsyganenko, N. A., Methods for quantitative modeling the magnetic field from Birkeland currents, *Planet. Space Sci., 39*, 641, 1991.

Tsyganenko, N. A., and A. V. Usmanov, Effects of the dayside field-aligned currents in location and structure of polar cusps, *Planet. Space Sci., 32*, 97, 1984

Usmanov, A. V., and N. A. Tsyganenko, An account of magnetic effects of the partial ring current system in quantitative modeling of geomagnetic field, *Geomagn. Aeron., 24*, 968, 1984.

Vasyliunas, V. M., Mathematical models of magnetospheric convection and its coupling to the ionosphere, In *Particles and Fields in the Magnetosphere*, edited by B.M. McCormac, p. 60, D. Reidel, Hingham, Mass., 1970.

N.A. Tsyganenko, Laboratory for Extraterrestrial Physics, Code 695, Goddard Space Flight Center, Greenbelt, Maryland 20771.